Soft Matter

PAPER

View Article Online
View Journal

Cite this: DOI: 10.1039/d6sm00167j

Effects of surface roughness on droplet impact dynamics

Joe Ghossein, *[a] Chinmay Kendurkar,[a] Jonathan B. Boreyko [b] and Olivier Coutier-Delgosha *[ac]

Past investigations into droplet impact dynamics have mostly used either relatively smooth substrates or air-trapping superhydrophobic textures. For this reason, existing models for predicting the maximum spreading ratio of impacting droplets ($\beta_{max} = D_{max}/D_0$) are unable to capture the influence of surface roughness. In this study, we investigate the influence of roughness and substrate wettability on the dynamics of water impacting at Weber numbers where splashing is minimal, with a specific focus on the maximal spreading diameter of Wenzel droplets. The surface mean roughness amplitude, R_a, was varied widely by laser etching substrates comprised of either glass (R_a = 0.012–22.49 μm), PETG (R_a = 1.18–55.04 μm), or aluminum (R_a = 2.21–58.31 μm). The surface wettability ranged from strongly hydrophilic to weakly hydrophobic and depended on the choice of substrate material, the extent of surface roughness, and the roughness-dependent modification of the intrinsic wettability due to the laser or hydrocarbon adsorption. We develop a new energy model for predicting β_{max} for both elastic (We $<$ 30) and inelastic (We $\geq$ 30) droplet impact regimes, where surface energy and viscous dissipation terms are modified to incorporate surface roughness effects. We show that the universality of existing (roughness-independent) models for β_{max} becomes incomplete for roughness ratios of $r \gtrsim 2$, whereas our roughness-dependent model has excellent agreement across all r values. By explicitly incorporating surface roughness into the energy balance, we extend the predictive capability of droplet spreading models to achieve an extended predictive framework for water-droplet spreading on rough substrates.

Received 26th February 2026,
Accepted 10th June 2026

DOI: 10.1039/d6sm00167j

rsc.li/soft-matter-journal

1 Introduction

Extensive studies have examined droplets impacting solid substrates in order to predict the maximal spreading diameter (D_{max}) when splashing does not occur. The corresponding maximal spreading ratio, $\beta_{max} = D_{max}/D_0$, where D_0 is the pre-impact droplet diameter is governed by how the droplet's initial kinetic energy is redistributed during impact. In the simplest physical picture, inertia drives the liquid radially outward, while viscous dissipation, surface-tension-driven creation of new interface, and contact-line wetting all oppose or redirect that motion. The relative importance of these effects depends on the liquid properties, impact velocity, and substrate characteristics, and is commonly expressed in terms of the Weber number (We), Reynolds number (Re), and wettability. On textured substrates, the situation becomes more complex because roughness can alter the true wetted area, promote pinning, and shift the droplet between Cassie–Baxter and Wenzel wetting states.[1,2]

According to Josserand & Thoroddsen,[1] viscosity, impact velocity, and surface tension play the dominant roles in setting β_{max}. Numerous models have been proposed, ranging from empirical fitting relations to theoretical expressions based on conservation of energy or momentum.

Early energy-balance models, such as that of Pasandideh-Fard *et al.*, incorporated viscous dissipation through a thin boundary-layer argument.[3] Physically, these models treat spreading as a competition between the droplet's initial inertia and the losses associated with near-wall shear and interfacial deformation. However, their treatment of wettability relied on the dynamic advancing contact angle as a surrogate for the intrinsic Young's angle, which can introduce inaccuracies, especially when contact-line dynamics are strong or when the substrate is not ideally smooth.

Ukiwe & Kwok[4] improved this framework by correcting the surface-energy term so that the equilibrium contact angle rather than the dynamic angle entered the model. Their formulation retains the same basic physics–inertia balanced

[a] Kevin T. Crofton Department of Aerospace and Ocean Engineering, Virginia Tech, Blacksburg, VA, USA. E-mail: joe20ghossein@vt.edu, ocoutier@vt.edu
[b] Department of Mechanical Engineering, Virginia Tech, Blacksburg, VA, USA
[c] CNRS, ONERA, Arts et Métiers ParisTech, Centrale Lille, FRE 2017 – LMFL, Laboratoire de Mécanique des Fluides de Lille, F-59000 Lille, France

against viscous dissipation and surface–energy increase, but treats the wetting term more consistently:

$$(\mathrm{We}+12)\beta_{\max}=8+{\beta_{\max}}^{3}\left(3(1-\cos\theta_{\mathrm{Y}})+4\frac{\mathrm{We}}{\sqrt{\mathrm{Re}}}\right) \quad (1)$$

Eqn (1) is implicit in $\beta_{\max}$, since $\beta_{\max}$ appears on both sides of the expression. Although physically motivated, it remains a semi-empirical smooth-surface model and does not explicitly account for roughness.

A different line of reasoning was developed by Laan *et al.*,[5] who focused on the crossover between two classical asymptotic limits: capillary-dominated spreading, for which $\beta_{\max} \propto \mathrm{We}^{1/2}$, and viscous-dominated spreading, for which $\beta_{\max} \propto \mathrm{Re}^{1/5}$. Adapting an interpolation scheme reported by Eggers *et al.*,[6] they obtained

$$\beta_{\max} \propto \mathrm{Re}^{1/5} f(\mathrm{WeRe}^{-2/5}), \quad (2)$$

where the argument $P \equiv \mathrm{WeRe}^{-2/5}$ acts as an impact parameter governing the crossover between capillary- and viscous-dominated spreading regimes. The strength of this approach is that it captures the transition between limiting mechanisms within one compact expression and gives excellent agreement for smooth substrates. Its limitation, however, is that roughness does not enter explicitly, so any roughness-dependent changes in wetted area, contact-line resistance, or viscous dissipation are necessarily folded into the scatter rather than resolved by the model.

More recent studies have sharpened the mechanistic understanding of droplet impact. Wildeman *et al.*[7] showed that, at sufficiently large Weber number, a geometric head-loss of approximately one-half of the initial kinetic energy provides a useful inertial baseline for spreading. Moitra *et al.*[8] emphasized the role of wettability energy barriers in governing spreading transitions, while Zhao *et al.*[9] and Lathia *et al.*[10] highlighted how improved diagnostics and surface design can modify spreading and contact time. Together, these studies reinforce that droplet impact is controlled not by a single universal mechanism, but by the interplay between inertia, viscous losses, surface-energy changes, and contact-line physics.

Although these advances have considerably improved the understanding of inertial, viscous, and capillary effects, the role of surface roughness in modulating $\beta_{\max}$ remains comparatively underexplored. Roughness is not merely a secondary geometric detail: it can increase the true solid–liquid interfacial area, enhance pinning, alter apparent wettability, and modify the dissipation pathways available during spreading. Prior studies have already pointed to these effects. Josserand & Thoroddsen[1] noted the difficulty of modeling droplet impact on micro-rough surfaces, while Vaikuntanathan & Sivakumar[11] and Yokoi *et al.*[12] showed that pinning and dynamic contact-angle changes can influence the maximal spread. Experiments by Quetzeri-Santiago *et al.*[13] and Zhao *et al.*[14] further demonstrated that roughness effects tend to be more pronounced on hydrophilic than on hydrophobic substrates. A later study by Singh *et al.*[15] attempted to incorporate roughness through a semi-empirical power-law relation,

$$\beta_{\max}=0.39\left(\frac{\mathrm{We}}{\mathrm{Oh}}\right)^{0.1}\left(\frac{R_{\mathrm{a}}}{D_0}\right)^{-0.065}, \quad (3)$$

where Oh is the Ohnesorge number and D_0 is the pre-impact droplet diameter. This correlation is useful in showing that roughness measurably affects spreading, but it remains empirical and was calibrated over a narrow range ($1 < \beta_{\max} < 2$). More importantly, it uses the line roughness amplitude R_{a}, which does not directly represent the actual wetted area that enters the surface-energy balance in a Wenzel state. Existing models such as eqn (1) and (2) provide strong mechanistic descriptions for smooth substrates but do not explicitly include roughness, whereas eqn (3) includes roughness only through a limited empirical fit. This leaves an important gap: a model that retains the physical structure of energy-based spreading dynamics while explicitly accounting for the way roughness modifies both wetting and dissipation. To address this, the present work seeks to develop a model incorporating the Wenzel roughness ratio (r) over a broad range of Weber numbers. Here, $r = A_{\mathrm{r}}/A$, where A_{r} is the roughened surface area and A is the projected surface area, both obtained through measurements using the Keyence VK-X3000 surface profiler.

Here, we characterize and model how the maximal spreading diameter, $\beta_{\max}$, varies with surface roughness and wettability. We first outline the selection and fabrication of our substrates in Section 2. In Section 3, we employ side-view high-speed imaging of droplet impact and spreading, measuring $\beta_{\max}$ for each sample. Finally, in Section 4 we propose a new roughness-based energy model for predicting $\beta_{\max}$ where the textured surface modulates the viscous dissipation and change in surface energy during spreading. While surface roughness is also known to affect splashing dynamics, the present study deliberately focuses on minimal-splashing impacts to extend the Laan model to rough surfaces while preserving its original analytical structure. In doing so, we revisit the assumptions underlying the Laan model, which, though widely adopted for its simplicity and generality, was not formulated to account for roughness. In contrast, real-world substrates, especially those engineered with nano- and micro-scale structures, can easily exceed this range of roughness. As we will show, while the Laan model continues to provide excellent global agreement across a wide range of Weber numbers, it does not explicitly account for surface roughness and therefore cannot resolve secondary roughness-dependent effects that emerge at intermediate impact velocities.

Although the absolute change in $\beta_{\max}$ with roughness is modest, it is systematic and experimentally resolvable, especially in the transitional regime. This is important because even a 5–10% separation in $\beta_{\max}$ is sufficient to produce clear roughness-dependent deviations from roughness-independent models, even when the curves remain close on a standard $\beta_{\max}$-versus-We plot. The objective of the present model is therefore not to claim a large global roughness effect at all Weber numbers, but rather to capture this reproducible secondary trend where existing formulations fail.

To account for both hydrodynamic regime changes and surface microtexture, we formulate a two branch predictive framework. The first branch corresponds to an elastic regime (We < 30) derived from the Richard & Quéré[16] and Okumura *et al.*[17] scaling, augmented by a roughness-dependent $\sqrt{r}$ correction and a finite zero-velocity spreading limit following the approach of Lee *et al.*[18]; In contrast to prior formulations employing a universal prefactor, the elastic-regime model introduces a material-dependent prefactor that reflects differences in substrate composition and surface processing. The second branch corresponds to an inelastic regime (We ≥ 30) that is a roughness-dependent extension from Wildeman's[7] head loss picture plus viscous dissipation. The choice of We = 30 as the crossover between the elastic and inelastic branches is physically motivated: it corresponds approximately to the onset of the fully developed lamella regime consistent with Wildeman's inertial head-loss picture, and is also supported by the present data, which show the strongest roughness-dependent deviations in the transitional window We $\sim$30–40 before weakening again at higher Weber number. Although the inelastic regime is governed by a fixed geometric head loss, roughness enters through its influence on both viscous dissipation and surface energy, allowing the model to remain weakly roughness-sensitive even at high Weber numbers. The resulting expressions are tested against the full experimental data set in Section 4.2.

A central challenge in modeling droplet impact on rough surfaces lies in defining an appropriate measure of wettability. On textured substrates, static apparent contact angles are not unique due to contact-line pinning and hysteresis, whereas advancing and receding contact angles are uniquely defined by force balance. In this work, quasi-static advancing contact angles are used as a physically motivated proxy to infer an effective Young's contact angle, enabling consistent incorporation of wettability effects into a roughness-dependent energy balance.

2 Methods

Deionized water droplets (density ρ = 997 kg m^{-3}, viscosity μ = 1.001 mPa s, and surface tension γ = 72.7 mJ m^{-2}) with pre-impact diameter D_0 = 2.10 $\pm$ 0.08 mm were generated using a micro-pump (New Era, Ne-500). Droplets were dispensed at 1200 μL min^{-1} (24–26 μL total volume) and detached under gravity. The impact velocity was controlled by adjusting the pump height, achieving V = 0.45–4.1 m s^{-1} (Re = 642–8061, We = 2.62–421). Detailed impact parameters are given in the Supplemental Material (Tables S4–S6). High-speed side-view imaging was performed with a Photron Fastcam SA1.1 camera (10 000 fps, 726 $\times$ 726 resolution) and LED backlighting. A Navitar Zoom 6000 lens ensured constant focus during zooming, with calibration performed before each run using a micro-calibration plate (LaVision). Background subtraction was employed to enhance droplet edge detection. Droplet diameter and velocity were measured using ImageJ software from the five frames preceding impact, with D_0 calculated as $(D_{vert}^2 D_{hor})^{1/3}$ following Rioboo *et al.*[19] Contact angles, height, and spread diameter during impact were extracted using an internal code based on perimeter detection with thresholding. Manual adjustment of thresholds and tangent points was occasionally required to account for lighting artifacts or droplet breakup. Each experimental condition was repeated three times to ensure statistical reproducibility. The reported values for the maximum spreading ratio β_{max} represent the average of these three independent trials. In all figures, the data points signify these mean values, while the error bars represent the standard deviation across the three trials.

Glass, PETG, and aluminum substrates were selected to systematically vary both material properties and surface roughness. Previous studies mostly examined droplet impacts on smooth surfaces without varying roughness extensively.[5,20] Although several reports measured β_{max} across different materials, no model incorporated roughness effects into β_{max} predictions.[19,21] In this work, roughness was widely varied, spanning mean amplitudes of R_a = 0.012–58.31 μm and peak amplitudes of R_p = 0.037–77.35 μm. Dynamic contact angles for each surface are listed in Table 1.

For each material, four roughness levels (3 for aluminum) were fabricated using laser etching, offering consistent and reproducible surface textures.[22] Surface profiles were measured using a Keyence VK-X3000 profiler ($\pm$1 + L/100 μm accuracy). Horizontal, vertical, and diagonal scans were averaged from five measurements per direction.

The line roughness (R_a) is not used as the primary model input because no universal mathematical relation exists between

Table 1 Line- and surface-based roughness parameters and mean advancing/receding contact angles (ACA-RCA) for all tested substrates. Roughness values were obtained using a Keyence VK-X3000 surface profiler, while contact angles were measured *via* the tilted substrate method. The Wenzel roughness ratio is given by $r = A_r/A$, where A_r is the roughened surface area and A is the projected surface area

Material	Sample	Wenzel roughness	R_a (μm)	R_p (μm)	Mean θ_a	Mean θ_r	CA. Hysteresis	θ_Y
Glass	1	1.00	0.012	0.037	68	14	54	68
	2	1.37	2.37	18.45	67	17	49	73
	3	1.59	6.50	23.31	64	9	55	74
	4	2.27	22.49	61.30	43	10	32	71
PETG	2	1.12	1.18	5.08	74	14	60	76
	3	1.13	9.61	16.80	63	20	43	66
	4	1.76	31.33	38.59	64	15	49	76
	5	2.17	55.04	80.40	53	21	32	74
Aluminum	2	1.84	2.21	12.19	71	11	60	80
	3	2.35	5.71	21.51	71	20	51	82
	4	6.35	58.31	99.58	125	96	29	95

R_a and the Wenzel roughness ratio r for real surfaces. Although R_a values are reported here for completeness and were extracted from three-dimensional surface measurements, R_a is still a one-dimensional amplitude metric and does not uniquely represent the actual wetted area relevant to Wenzel wetting. By contrast, r directly measures the ratio of actual to projected surface area. Conventional stylus-based line measurements can also under-resolve narrow grooves because of finite tip size and direct surface contact, further limiting its usefulness.

Glass substrates (50 × 75 mm^2, 6 mm thick, initial R_a = 0.012 μm) were etched using a CO_2 laser (Epilog Zing-24) to create random, fused surface textures (Fig. 1(b–d)). PETG samples (50 × 50 mm^2) were molded by heating Overture PETG filament (1.24 g cm^{-3}, T_{melt} = 230 °C) and subsequently laser-etched. Initial PETG roughness (R_a = 1.13 μm) exceeded that of smooth glass, thus only the four roughened PETG samples were tested. Etching produced uniform, circular roughness elements (D ∼ 276 μm), as shown in Fig. 1(e–h). Aluminum 3003-H14 plates (50 × 50 mm^2) were etched using a fiber laser (Boss-FM30). Initial roughness (R_a = 1.42 μm) similarly precluded testing unetched surfaces. Depending on laser settings (see Table S3), surfaces exhibited either melted, disordered textures (R_a = 5.71 μm; Fig. 1(i)) or structured square roughness patterns (R_a = 58.31 μm, spacing ∼107 μm; Fig. 1(l)). The laser parameters and corresponding roughness measurements for all substrates are provided in the SI (Tables S1–S3).

Quasi-static advancing and receding contact angles (ACA-RCA) were simultaneously measured using the tilted plate method,[23] wherein a water droplet on a horizontal substrate is slowly tilted until sliding initiates. The leading and trailing edges of the droplet correspond to the advancing and receding contact angles, respectively. The experimental setup was identical to that used for droplet impact measurements, except that the substrate was mounted on a Velmex B4872TS rotary table (0.025° precision).

On rough and chemically heterogeneous surfaces, static apparent contact angles are not uniquely defined due to contact-line pinning and hysteresis, and multiple equilibrium configurations may coexist for the same droplet volume. In contrast, advancing and receding contact angles measured under quasi-static conditions are uniquely determined by a force balance at the contact line. For this reason, quasi-static advancing contact angles (ACA) obtained from the tilted-plate method are used in the present study as a physically motivated proxy for wettability. These ACA values are subsequently employed to infer an effective Young's contact angle through the Wenzel relation when required for model inputs.

In addition to the present experiments, independently published droplet impact data on rough steel substrates from Singh *et al.*[15] are used exclusively to assess the elastic impact regime (We <30), as their data do not extend to higher Weber numbers. The assumptions required for incorporating these data are discussed explicitly in Section 4.1.

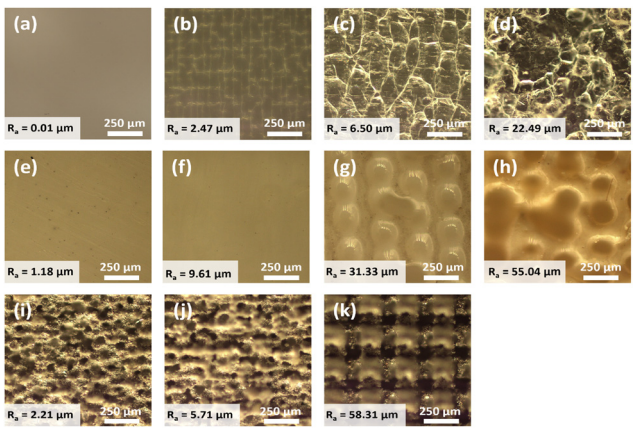

Fig. 1 Roughness height profile images showcasing the surfaces of the smooth (a) and laser etched glass (b)–(d), PETG (e)–(h), and aluminum (i)–(l) and obtained by scanning the surfaces in 3D using the Keyence VK-X3000.

3 Experimental results

3.1 Mean ACA-RCA across all substrates

Advancing and receding contact angles (ACA-RCA) were measured using the tilted-plate method, with mean values summarized in Table 1. Standard deviations across glass (2.0° for θ_a, 0.6° for θ_r), PETG (3.0°, 1.5°), and aluminum (2.4°, 0.7°) indicate consistent measurements.

On hydrophilic glass, ACA decreased slightly with increasing roughness, while RCA remained relatively stable. Similar muted trends were observed for PETG and aluminum, where ACA and RCA either decreased modestly or even increased with roughness. Notably, roughened aluminum exhibited hydrophobic apparent contact angles (θ_a = 125°, θ_r = 96°). These results seemingly contradict the Wenzel equation:

$$\cos\theta^* = r\cos\theta_Y, \tag{4}$$

which predicts a monotonic decrease of θ^*, the apparent static contact angle on the roughened surface with increasing roughness for hydrophilic materials.

The measured advancing and receding contact angles do not exhibit a monotonic dependence on surface roughness and do not follow the trends predicted by the Wenzel relation when assuming a constant intrinsic contact angle. Instead, the intrinsic Young's contact angles (θ_Y) inferred from the quasi-static advancing contact angle using the Wenzel relation (Table 1) vary across both material type and roughness level. For glass substrates, the inferred Young's contact angle increases from approximately 68° for the smooth surface to values in the range of 71–74° for the roughened samples, while for PETG it spans approximately 66–76° across the tested roughness range. For aluminum, the inferred Young's contact angle increases from approximately 80° for moderately rough surfaces to approximately 95° for the most highly roughened sample for which contact angles could be measured.

These variations suggest that the intrinsic wettability of the substrates is modified by the laser texturing process itself, consistent with prior reports of roughness-induced structural[24] and chemical surface modifications.[25] In addition, adsorption of

atmospheric volatile organic compounds (VOCs) following laser processing has been shown to increase intrinsic hydrophobicity and, in some cases, convert hydrophilic surfaces into hydrophobic ones.[26,27] Taken together, these observations indicate that surface roughness alone is insufficient to characterize wettability and that the effective intrinsic contact angle varies across the laser-processed substrates.

Complete decoupling of roughness and intrinsic wettability is not generally possible for laser-processed surfaces, since the texturing process itself can modify surface chemistry in addition to topography. Nevertheless, the variation in the inferred θ_Y values is relatively small for the glass and PETG substrates, changing from 68° to 71° for glass and from 76° to 74° for PETG across the tested roughness range, so the roughness dependence remains clearly identifiable for this subset of the data.

3.2 Effects of roughness on impact dynamics

A range of impact phenomena were observed depending on substrate and conditions (see Tables S4–S6). Splashing behaviors varied markedly with surface roughness and Weber number (We), as visualized in Fig. 2. Minor splashing with negligible mass loss occurred on moderately roughened glass (sample 3) and PETG (samples 2 and 3) for We $\gtrsim$ 300. Appreciable splashing—characterized by radial droplet ejection—appeared on rough PETG (samples 4 and 5) for We $>$ 100, coincident with liquid interaction with circular roughness elements (see Fig. 1). Shattering, where the bulk droplet fragmented, was observed for heavily roughened glass, PETG, and all aluminum surfaces for We $>$ 100. In some cases, shattered droplets partially reassembled during retraction. For all subsequent analysis of β_{max}, only cases with no or negligible splashing were considered.

Droplet dynamics without splashing were distinct across materials. At low Weber numbers (We $\sim$ 1) on glass, impacts produced a staircase morphology across all roughness levels (Fig. 3(a)). Increasing We $\sim$ 10 triggered Worthington jets (without droplet ejection) for smooth and moderately rough glass (samples 1–3) (Fig. 3(b)). At higher We $\sim$ 100, droplets transitioned to deposition behavior; heavily roughened glass (sample 4) approached complete wetting (Fig. 3(c)).

PETG surfaces showed greater resilience to wetting compared to glass. Staircase structures and Worthington jets were still observed at low We $\sim$ 1–10, often accompanied by early or late droplet ejection depending on roughness (Fig. 4). Notably, PETG avoided full surface wetting even at higher roughness levels, consistent with its roughness topography facilitating reduced liquid–solid contact.

Aluminum substrates, distinguished by hydrophobicity at high roughness, showed full rebound across R_a = 2–58 μm for We $\sim$ 1–10 (Fig. 5(a and b)). Single-volume rebound occurred at low We, while daughter droplet ejection accompanied rebounds at intermediate We. At We $\gtrsim$ 150, even shattered droplets partially recoiled, indicating transient partial-Cassie states despite nominal surface hydrophilicity at rest. Overall, roughness intensified splashing tendencies, shifted rebound dynamics, and altered spreading outcomes, underscoring its critical role beyond simple wettability changes.

Fig. 2 Different splashing behavior of water impacting (a) glass (R_a = 6.50 μm, We = 300), (b) PETG (R_a = 31.33 μm, We = 315), and (c) aluminum (R_a = 58.31 μm, We = 314). For similar We numbers, (a) tiny amount of side-splash is observed upon impact on glass, (b) a large radial ejection is observed for PETG, (c) and a complete breakup of the droplet is seen for aluminum.

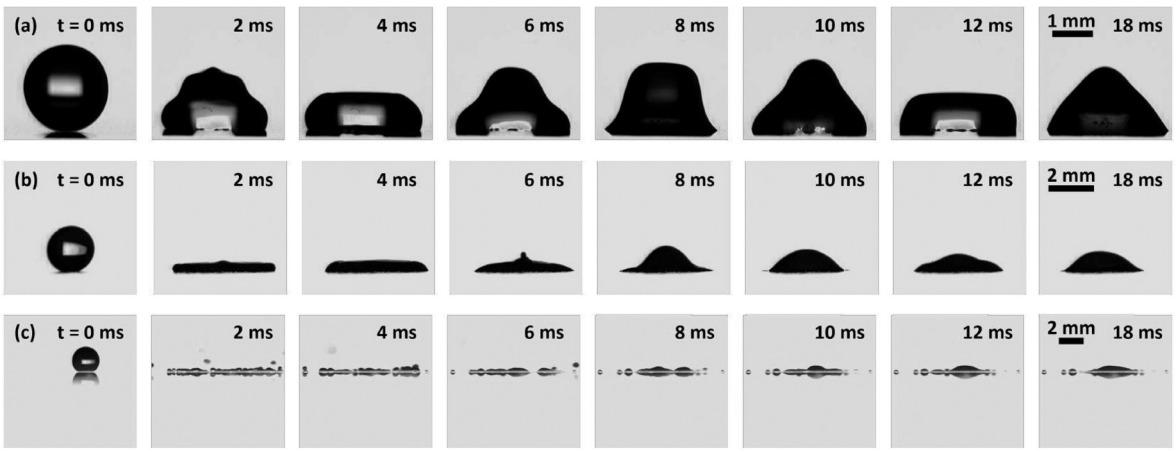

Fig. 3 Single 2 mm droplet impact on glass for (a) sample 2 with V = 0.31 m s^{-1} demonstrating staircase behavior, (b) sample 3 with V = 1.11 m s^{-1} exhibiting the formation of a Worthington jet, and (c) sample 4 with V = 2.38 m s^{-1} demonstrating splash. t = 0 ms denotes the time of impact.

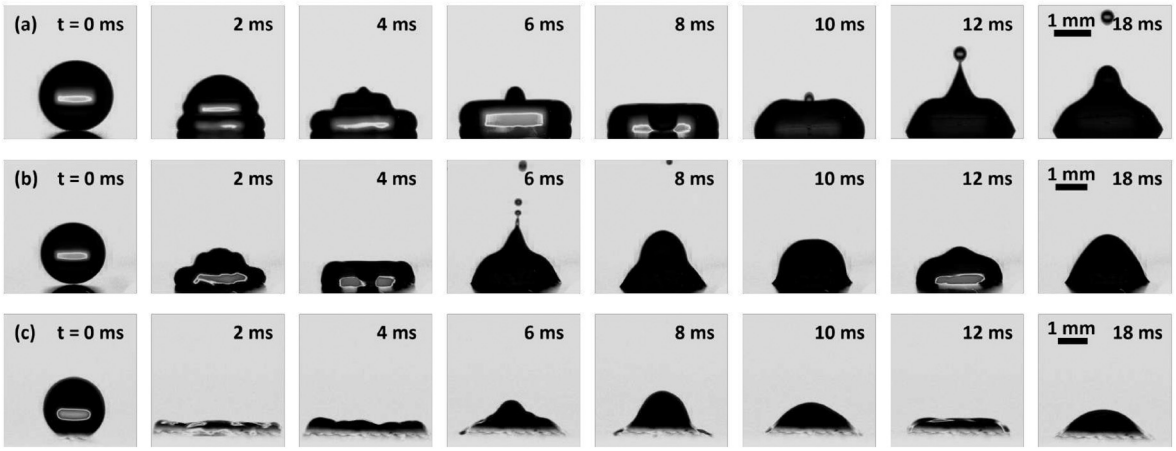

Fig. 4 Single 2 mm droplet impact on PETG for (a) sample 2 with V = 0.36 m s^{-1} demonstrating staircase and late (t = 12 ms) droplet ejection, (b) sample 4 with V = 0.36 m s^{-1} demonstrating early (t = 6 ms) droplet ejection, and (c) sample 5 with V = 1.21 m s^{-1} demonstrating deposition. t = 0 ms denotes the time of impact.

4 Variations in the maximum spreading rate

While several models for β_{max} exist, none incorporate surface roughness effects. Fig. 6 presents the variation of β_{max} with Weber number (We) and roughness for all materials. Because all experiments in the present study were performed with deionized water, We and Re were varied only through the impact velocity and were therefore not independently controlled. The present model validation is accordingly restricted to water droplets, and extension to liquids of substantially different viscosity or surface tension will require further experimental assessment. Here, cases involving significant splashing or droplet breakup were excluded from analysis to ensure β_{max} could be meaningfully compared across varying roughness and Weber numbers. As expected, β_{max} increases monotonically with We, consistent with prior studies.[1,21,28,29] Roughness also appreciably influences β_{max}: at We $\sim$ 40, roughness altered β_{max} by 10.6% for glass (Fig. 6a), 8.0% for PETG, and $-$2.8% for aluminum (Fig. 6c). In other words, the largest β_{max} values occurred on the smoothest surfaces for glass and PETG, but on the the roughest surfaces for aluminum. The effect of roughness on β_{max} was more prominent at lower velocities where We $<$ 100.

Roughness also mattered in terms of causing complete wetting or splashing for We $>$ 100, where β_{max} is no longer a measurable concept in contrast to the smoother surfaces. Using the case of We $\sim$ 160, for example, β_{max} could not be measured for glass when using the R_a = 22.49 μm sample, PETG for R_a = 31.33 μm, and aluminum even for the smoothest case of R_a = 2.21 μm.

4.1 Elastic-regime (We $<$ 30): modified Richard-Okumura law with finite wetting correction

At sufficiently low Weber numbers, droplet impact is approximately elastic: the drop deforms weakly and, in the ideal limit, rebounds without forming a thin lamella or an extended viscous film.[16,17] In this regime, Richard and Quéré[16] and Okumura *et al.*[17] showed that, for an ideal, smooth, and non-wetting substrate, the maximum spreading factor obeys the

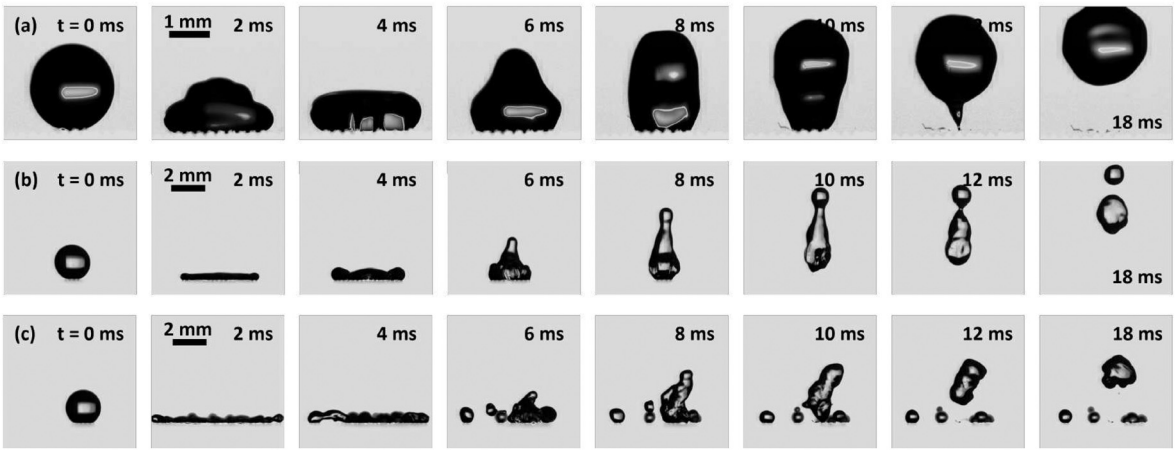

Fig. 5 Single 2 mm droplet impact on aluminum demonstrating (a) full rebound for sample 2 with V = 0.41 m s^{-1}, (b) full rebound and droplet ejection for sample 4 with V = 1.18 m s^{-1} and (c) shattering followed by a large droplet ejection for sample 4 with V = 2.38 m s^{-1}. t = 0 ms denotes the time of impact.

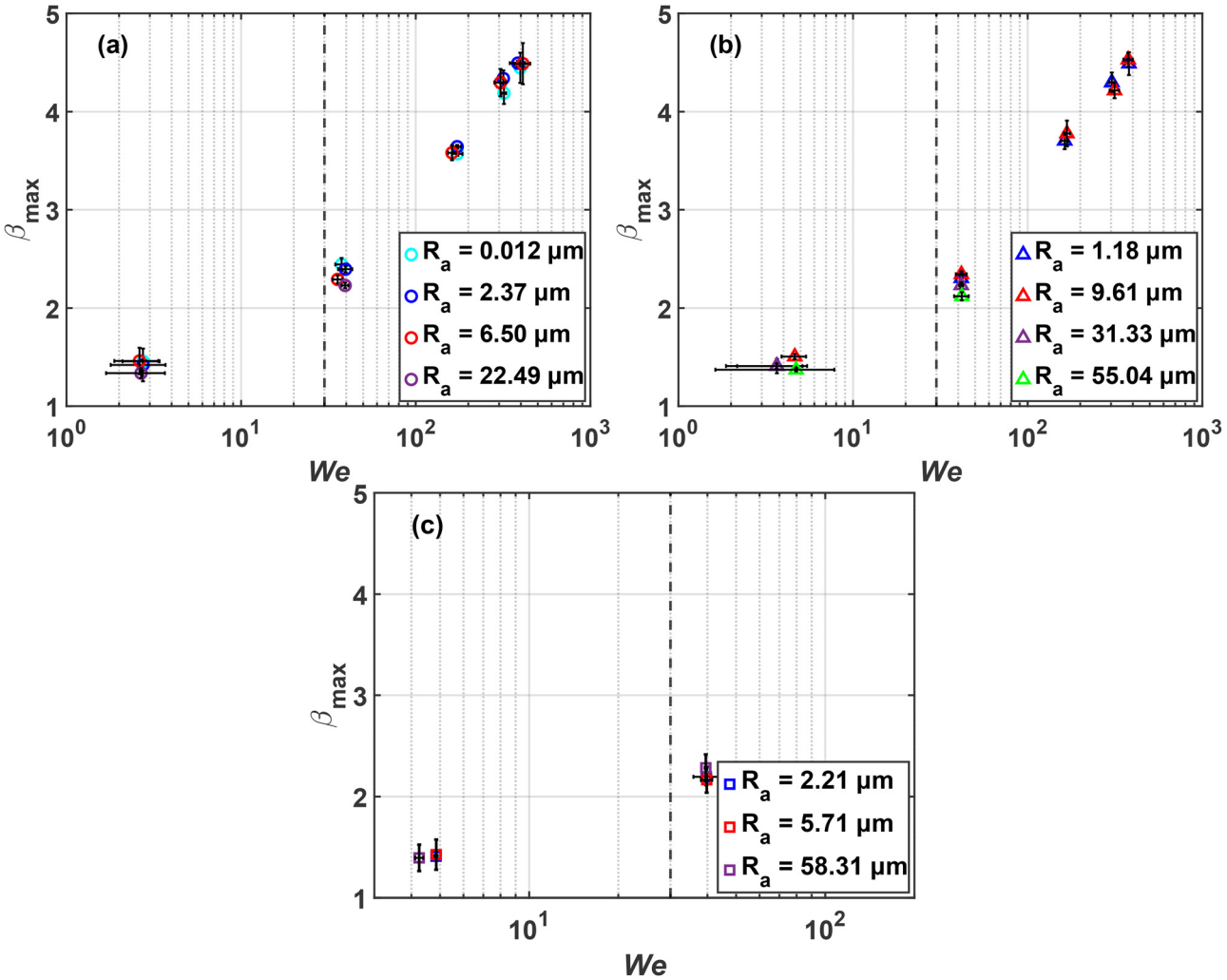

Fig. 6 β_{max} variation plotted for (a) glass, (b) PETG, and (c) aluminum substrates for $1 < We < 420$. The data cuts off due to splashing or complete penetration of the substrate for the case of (a) glass with R_a = 22.49 μm ($We > 30$), (b) PETG with R_a = 31.33 μm–R_a = 55.04 μm ($We > 30$), and (c) aluminum for all cases where $We > 30$. The dashed line denotes $We = 30$. Data points represent the average of three experimental trials, with vertical error bars indicating the standard deviation in β_{max}, while horizontal error bars indicate the standard deviation in We.

capillary–elastic scaling

$$\beta_{max} - 1 \propto \sqrt{We}. \quad (5)$$

This scaling can be recovered by balancing the initial kinetic energy of the impacting droplet against the capillary energy stored at maximum deformation. Writing the droplet kinetic energy as $E_k \sim \rho {D_0}^3 {V_i}^2$ and the capillary deformation energy as $E_\gamma \sim \gamma {D_0}^2({\beta_{max}}^2 - 1)$, one obtains

$$E_k \sim E_\gamma \Rightarrow \rho {D_0}^3 {V_i}^2 \sim \gamma {D_0}^2({\beta_{max}}^2 - 1), \quad (6)$$

which yields eqn (5) after introducing the Weber number.[16,17] This argument assumes that (i) the substrate is chemically homogeneous, (ii) its topography is sufficiently smooth that the drop interacts primarily with the projected area, and (iii) the dominant surface-energy change arises from deformation of the liquid–vapor interface rather than from wetting of the substrate.

For wetting substrates, eqn (5) reduces to $\beta_{max} \to 1$ as $We \to 0$; however, this is not physically realistic. Even in the limit of vanishing impact velocity, a droplet spreads to a finite diameter determined by capillarity and wettability. In particular, B_0 is not generally expected to equal 1 on wetting substrates, because a droplet deposited with negligible impact velocity still relaxes to a finite sessile-cap footprint whose diameter is set by capillarity and wettability and may exceed the initial free-drop diameter D_0. Following Lee *et al.*,[18] we therefore introduce a finite zero-velocity spreading limit

$$B_0 \equiv \lim_{V_i \to 0} \beta_{max}, \quad (7)$$

which represents the capillary spreading ratio in the absence of impact inertia. In the present work, B_0 is obtained for each material from the zero-impact-velocity limit using the procedure of Lee *et al.*,.[18] It is therefore convenient to define the inertial increment above this wetting baseline as

$$\Delta\beta \equiv \beta_{max} - B_0 \quad (8)$$

With this definition, the smooth-surface elastic scaling becomes

$$\Delta\beta \propto \sqrt{We} \quad (9)$$

On rough, wettable substrates the droplet impales the texture and spreads in a Wenzel state. Two additional effects must then be considered: geometric roughness and substrate wettability. The true solid–liquid interfacial area exceeds the projected area by the Wenzel roughness ratio $r = A_r/A$. Since r is an area ratio whereas β_{max} is a length ratio, the corresponding first-order geometric correction to the spreading length is taken to scale as $\sqrt{r}$. In other words, $\sqrt{r}$ is introduced here as a geometric length-scale correction associated with the increase in available wetted interfacial area under Wenzel wetting.

The second correction arises from wettability. In the Young–Wenzel framework, the wetting contribution to the interfacial energy depends on $\cos\theta_Y$, where θ_Y denotes the effective Young's contact angle used as the model input. For hydrophilic substrates, $\cos\theta_Y > 0$, so increased wettability lowers the energetic cost of wetting and promotes additional spreading. Accordingly, the incremental spreading above the baseline B_0 is taken to scale to first order as

$$\Delta\beta \propto \sqrt{r}\cos\theta_Y\sqrt{We}. \quad (10)$$

Introducing a material-dependent prefactor κ to account for differences in substrate chemistry and surface processing gives

$$\Delta\beta = \kappa\sqrt{r}\cos\theta_Y\sqrt{We}. \quad (11)$$

Substituting eqn (8) into eqn (11) yields the elastic-regime model used in the present work:

$$\beta_{max} = B_0 + \kappa\sqrt{rWe}\cos\theta_Y \quad (We < 30). \quad (12)$$

Eqn (12) should therefore be interpreted as a physics-informed scaling extension of the Richard–Okumura elastic law to hydrophilic Wenzel-type impacts, rather than as a strict first-principles derivation. The term B_0 accounts for the finite wetting-controlled spreading at zero impact velocity, the factor $\sqrt{r}$ represents the first-order geometric correction associated with roughness-enhanced interfacial area, and $\cos\theta_Y$ provides the corresponding first-order wettability correction motivated by Young–Wenzel interfacial energetics.

Here, κ is a material-dependent prefactor that captures the influence of substrate chemistry and surface processing on elastic spreading. In contrast to prior formulations employing a universal prefactor, κ is determined independently for each substrate material by maximizing the coefficient of determination between experimentally measured and predicted spreading ratios in the elastic regime. The fitted value of κ for glass, PETG, aluminum, and steel is reported in Table 2.

Eqn (12) forms the first branch of the piecewise model proposed in this work. As a consistency check, we also compare the elastic-regime scaling against independent low-Weber-number data for rough steel substrates reported by Singh *et al.*[15] Because those experiments are restricted to We <30, they provide a useful test of whether the proposed first-order $\sqrt{r}$ correction captures the leading geometric roughness effect in the weak-deformation Wenzel regime. Although the mechanically processed steel surfaces in Singh *et al.* differ morphologically from the laser-etched surfaces studied here, both studies quantify roughness through the ratio of actual to projected surface area. Once the droplet is assumed to penetrate the texture and spread in a Wenzel state, this area ratio is the relevant first-order geometric quantity controlling the increase in wetted interfacial area. The comparison should therefore be interpreted as support for using r as a first-order Wenzel-state roughness descriptor in the elastic regime, rather than as proof that all topology-dependent effects are absent. For the steel substrates, the effective Young's contact angle θ_Y used in eqn (12) is inferred from literature values for water–steel systems, together with the relatively weak dependence of intrinsic wettability on roughness for etched steel surfaces.

Table 2 Material-dependent values of the elastic-regime prefactor κ used in eqn (12)

Material	Glass	PETG	Aluminum	Steel (Singh *et al.*[15])
κ	0.51	0.54	0.70	0.77

The choice of We = 30 as the crossover between the elastic and inelastic branches is physically motivated: it corresponds approximately to the onset of the fully developed lamella regime identified by Wildeman *et al.*[7] and is also consistent with the present data, where the strongest roughness-dependent deviations occur in the transitional range We $\sim$ 30–40 before weakening again at higher Weber number.

Notably, while our energy-based framework successfully unifies both our experimental data and those of Singh *et al.*,[15] the empirical model originally proposed by those authors fails to scale accurately outside of its calibration regime. As detailed in Fig. S1 and Section S2 of the SI, the Singh model significantly under-predicts the spreading ratios for the higher-velocity impacts investigated in this study, further justifying the necessity of the proposed bimodal physical scaling.

Fig. 7 compares the experimentally measured maximum spreading ratios with predictions from the elastic-regime model for both the present data set and the independent steel data reported by Singh *et al.* The reported coefficient of determination, $R^2 = 0.91$, is computed from this combined parity plot and therefore reflects the agreement across all elastic-regime points shown in the figure. In this comparison, the prefactor κ is fitted per material, yielding four values in total (glass, PETG, aluminum, and steel), while the zero-velocity spreading limit B_0 is fitted per surface, yielding sixteen values across the roughness levels included in Fig. 7.

4.2. Inelastic-regime (We $\geq$ 30): roughness effects in inertia-dominated spreading

Currently, several predictive models for β_{max} exist for We $\geq$ 30. These models balance inertial, capillary, and viscous forces, yielding scaling laws based on Reynolds, Ohnesorge, and Weber numbers. Various assumptions underpin these models:

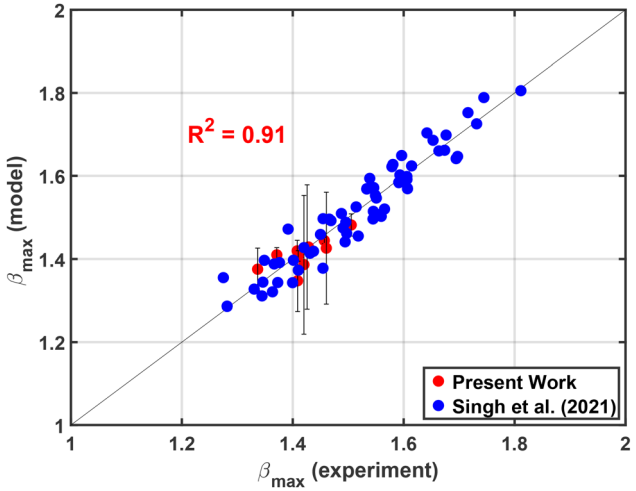

Fig. 7 Comparison between experimentally measured and model-predicted maximum spreading ratios in the elastic regime (We < 30). Red symbols correspond to the present experiments on glass, PETG, and aluminum substrates, while blue symbols correspond to independent low-Weber-number data for rough steel substrates reported by Singh *et al.*[15] The solid line indicates perfect agreement (β_{max}(model) = β_{max}(experiment)). The reported R^2 = 0.91 is computed from the combined present-plus-Singh data shown here; The comparison uses material-dependent κ values (0.51, 0.54, 0.70, and 0.77 for glass, PETG, aluminum, and steel, respectively) and surface-dependent B_0 values obtained from the zero-impact-velocity limit for each surface.

surfaces are often taken as superhydrophobic,[28] viscous boundary layers are emphasized,[29] or energy balances are made assuming smooth substrates.[4] While highly successful for smooth and weakly textured substrates, most existing formulations do not explicitly incorporate surface roughness effects.

Building upon these frameworks, Laan *et al.*[5] presented a widely adopted interpolation model that bridges capillary-dominated ($\beta_{max} \propto We^{1/2}$) and viscous-dominated ($\beta_{max} \propto Re^{1/5}$) spreading regimes using an approach inspired by Eggers *et al.*[6] Their scaling interpolates between these limits as

$$\frac{D_{max}}{D_0} \propto Re^{1/5} f_{EC} \quad \left(WeRe^{-2/5}\right) \tag{13}$$

where f_{EC} is a function of $WeRe^{-2/5}$ that varies between zero in the capillary regime and infinity in the viscous regime. An impact parameter $P \equiv WeRe^{-2/5}$ is defined to distinguish between capillary- and viscous-dominated regimes, and using a [1,1] Padé approximation, Laan *et al.*[5] created a smooth crossover:

$$(D_{max}/D_0)Re^{-1/5} = P^{1/2}\left(A + P^{1/2}\right) \tag{14}$$

where $A = 1.24 \pm 0.01$ is a fitting constant.

When applied to the present data set for We ≥ 30, the Laan model yields strong overall agreement with the measured spreading ratios. Using the original prefactor A = 1.24 proposed by Laan *et al.*, the resulting coefficient of determination between experimentally measured and model-predicted β_{max} values is R^2 = 0.97 when the comparison is restricted to the inertial regime. This level of agreement is consistent with the inertia-dominated nature of high-Weber-number spreading, where global kinematics largely govern the maximum spread.

Consistent with the trends observed in Fig. 6, the influence of surface roughness on maximal spreading is most pronounced in the intermediate Weber-number range around We ∼ 40, where the largest separation in β_{max} between smooth and rough substrates is observed. This behavior is reflected in Fig. 8, where the legend denotes each substrate (glass, PETG, and aluminum) by its initial, with the specific sample identified by a subscript corresponding to Table 1. Despite the strong global performance of the Laan model, closer inspection reveals systematic deviations in this intermediate regime (30 < We < 60), where data corresponding to different roughness levels collapse toward similar predicted values even though the experimental measurements remain measurably separated. This indicates that surface roughness effects are not captured when inertial and surface contributions are of comparable magnitude. Similar deviations at low and intermediate Weber numbers were previously noted by Lee *et al.*,[18] who introduced a finite-volume correction for smooth and weakly textured substrates, though without explicitly accounting for surface roughness. As the Weber number increases further, air entrapment and inertial dominance reduce the sensitivity of β_{max} to surface roughness, leading to improved agreement between roughness-independent models and experimental data. Although the corresponding shifts in β_{max} are modest in absolute magnitude, they are sufficiently systematic to produce visible parity-plot deviations from the roughness-independent model, which is why the transitional regime rather than the high-We limit provides the most meaningful test of roughness sensitivity.

Motivated by the shortcomings, we developed an alternative model that incorporates surface roughness explicitly within an energy conservation framework. We begin by balancing the droplet's initial kinetic energy, E_k, with viscous dissipation, E_μ, and changes in surface energy, ΔE_S:

$$E_k = \Delta E_S + E_\mu \tag{15}$$

The droplet is initially spherical, with diameter D_0 and impact velocity V_0, yielding an initial kinetic energy:

$$E_k = \frac{\pi}{12}\rho {D_0}^3 {V_0}^2 \tag{16}$$

Surface energy changes are more subtle. Initially, the total energy is the sum of the droplet's surface energy and the dry substrate surface energy, expanded by the roughness factor r:

$$E_{Si} = \pi\gamma {D_0}^2 + \frac{\pi}{4}\gamma_{sg} {D_{max}}^2 r \tag{17}$$

where γ_{sg} is the solid–gas interfacial tension. At maximum spreading (pancake shape), the surface energy becomes:

$$E_{Sf} = \pi\gamma\left(\frac{{D_{max}}^2}{4} + D_{max}h\right) + \frac{\pi}{4}\gamma_{sl} {D_{max}}^2 r \tag{18}$$

where γ_{sl} is the solid–liquid interfacial tension and where h is

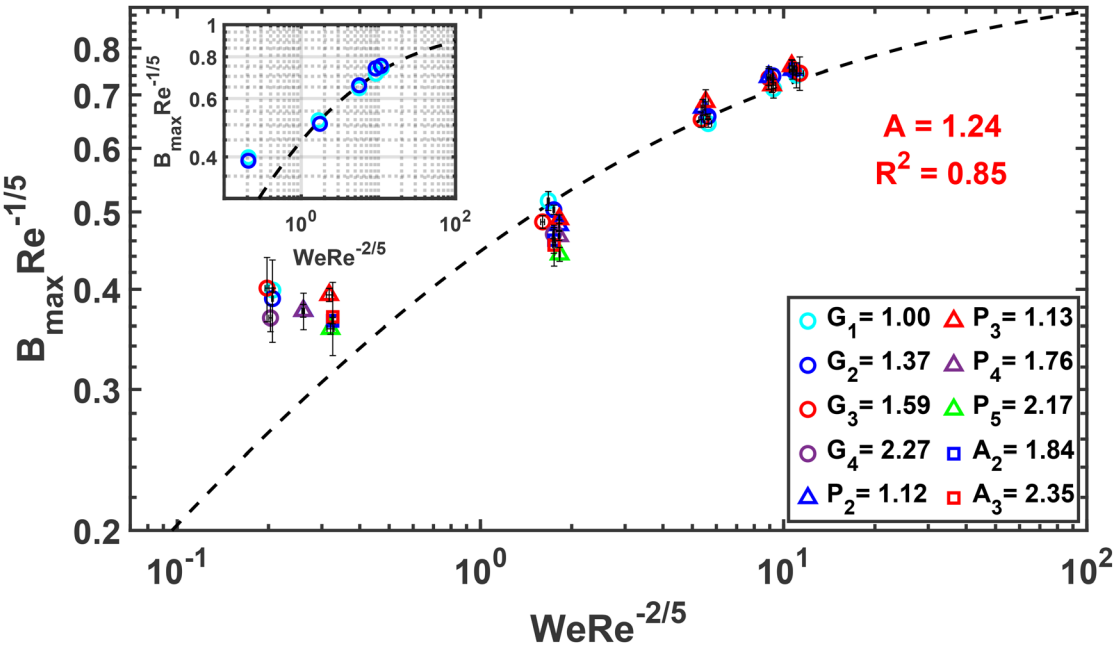

Fig. 8 Curve showing the model by Laan *et al.*[5] (dashed line) plotted against the present experimental data. For the entire data set $1 < We < 420$, the coefficient of determination between experimentally measured and model-predicted β_{max} values is $R^2 = 0.85$, whereas restricting the comparison to the inertial regime $We \geq 30$ raises the fit to $R^2 = 0.97$. The leftmost cluster corresponds to elastic-regime impacts ($We < 30$), while the remaining clusters correspond to inertia-dominated impacts ($We \geq 30$). The inset displays data from glass samples 1 and 2, highlighting the model's closer agreement for low-roughness glass substrates. The legend denotes each substrate through its initial with the specific sample denoted by the subscript matching the data in Table 1.

the pancake thickness:

$$h = \frac{2}{3}\frac{{D_0}^3}{{D_{max}}^2} \tag{19}$$

The interfacial tensions are linked by Young's law:

$$\cos\theta_Y = \frac{\gamma_{sg} - \gamma_{sl}}{\gamma} \tag{20}$$

where θ_Y is that of each substrate as noted in Table 1. However, the initial surface energy of the droplet before impact is typically negligible compared to kinetic energy at high Weber number, and the spreading dynamics "forget" the droplet's initial surface energy. Thus, we simplify the initial system energy to be purely that of the rough dry substrate:

$$E_{Si} = \frac{\pi}{4}\gamma_{sg}{D_{max}}^2 r \tag{21}$$

ΔE_S is obtained by substituting eqn (19) into eqn (18) and subtracting eqn (21) from it.

$$\Delta E_S = \pi\gamma {D_0}^2\left[\frac{{D_{max}}^2}{4{D_0}^2} + \frac{2D_0}{3D_{max}} - \frac{{D_{max}}^2 r\cos\theta_Y}{4{D_0}^2}\right] \tag{22}$$

The inelastic-regime model is formulated under the assumption that the droplet remains in a Wenzel-type wetting state during spreading, such that the liquid conforms to the roughened substrate and the wetted interfacial area scales with the roughness ratio r. Accordingly, the model is intended for surfaces and impact conditions for which full penetration of the texture is a reasonable approximation, and it is not intended to describe Cassie or mixed Cassie–Wenzel states.

Notably, while the dynamic contact angle may deviate from θ_Y at high velocities, this kinematic variation does not affect our model as the pancake approximation (eqn (18)) defines the liquid–air area through volume conservation rather than the contact angle. Furthermore, at $We > 300$, the surface energy contribution is an order of magnitude smaller than the kinetic and viscous terms (Fig. 9), making the spreading dynamics insensitive to dynamic wetting discrepancies in the high-inertia limit.

To model the viscous energy, we account for the dissipation that develops in the near-wall shear layer during spreading. Building on the analysis of Wildeman *et al.*,[7] we assume that for fully developed inelastic impacts at high Weber number ($We \geq 30$), approximately half of the initial kinetic energy is lost through a geometric "head-loss", while additional dissipation arises from shear in the near-wall boundary layer. The term $E_k/2$ is therefore used as a first-order inertial baseline, not as an exact universal constant; on rough substrates, deviations from one-half may occur because roughness can perturb the large-scale lamella and rim dynamics. In the present framework, such departures are not modeled separately and are absorbed indirectly into the additional viscous correction and fitted prefactor. Hence, the total dissipative contribution is written as

$$E_\mu = E_d^{BL} + \frac{E_k}{2} \tag{23}$$

In the Wildeman *et al.*[7] and Pasandideh-Fard *et al.*[3] framework, E_d^{BL} is estimated from a scaling argument in which a

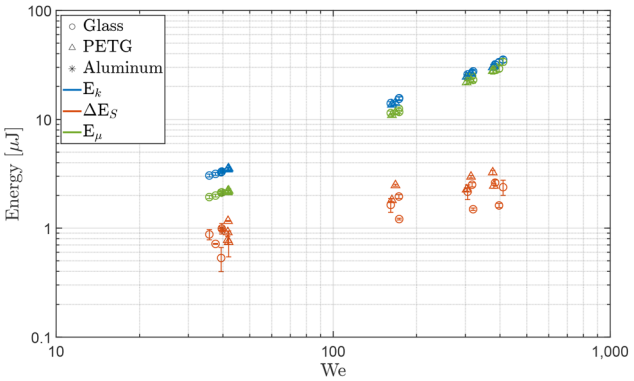

Fig. 9 Order-of-magnitude comparison of the initial kinetic energy E_k, the total surface-energy change ΔE_S, and the total dissipative contribution E_μ over the inertial impact regime (We ≥ 30). Here, ΔE_S corresponds to the surface-energy contribution defined in eqn (22), while E_μ is the total dissipative term defined in eqn (24). The first two terms on the right-hand side of eqn (25) are both contained within ΔE_S, whereas the third term corresponds to the additional roughness-amplified boundary-layer dissipation. Across the present experimental range, E_k and E_μ remain of comparable magnitude, while ΔE_S is consistently smaller, indicating that inertia and dissipation dominate the overall energy budget once the lamella is fully developed.

shear boundary layer of thickness $H_b \sim \sqrt{\nu t}$ develops near the wall as the droplet spreads radially. The associated dissipation scales as $\mu\,(V_0/H_b)^2(D_{max}{}^2H_b)\tau_m$, where τ_m is the spreading time. Using the usual estimate $\tau_m \sim D_0(\beta_{max}-1)/V_0$, this gives the familiar boundary-layer scaling $E_d^{BL} \propto \beta_{max}{}^2\sqrt{\beta_{max}-1}E_k/\sqrt{Re}$.

When accounting for substrate roughness, we propose that the primary effect of roughness on viscous dissipation is not to increase dissipation directly in proportion to the roughened area, but rather to modify the effective momentum-diffusion length within the boundary layer itself. Specifically, local asperities perturb the near-wall flow through obstruction, recirculation, and reattachment, which enhances shear and reduces the effective viscous penetration length. To represent this effect in the simplest first-order manner, we introduce a roughness-modified boundary-layer thickness $H_{b,r} \sim H_b/\sqrt{r}$. Because r is an area ratio whereas H_b is a length scale, the roughness correction enters the viscous term through $\sqrt{r}$ rather than r. Substituting $H_{b,r}$ into the boundary-layer dissipation estimate therefore yields a roughness-amplified viscous term proportional to $\sqrt{r}\beta_{max}{}^2\sqrt{\beta_{max}-1}E_k/\sqrt{Re}$, which is then added to the geometric head-loss contribution of $E_k/2$. Overall, the viscous dissipation is modeled as

$$E_\mu = \alpha\frac{\sqrt{r}\beta_{max}{}^2\sqrt{\beta_{max}-1}}{\sqrt{Re}}E_k + \frac{E_k}{2} \qquad (24)$$

where α is an $O(1)$prefactor reflecting the precise velocity profile and the idealized nature of the boundary-layer closure. In the inelastic regime, a single prefactor α is obtained by fitting the model to the full We ≥ 30 data set across all materials. This reflects the reduced sensitivity of inertia-dominated spreading to material-specific wettability and surface chemistry, in contrast to the elastic regime where such effects are more pronounced. We further note that moving-contact-line dissipation is not modeled separately here and is instead absorbed only indirectly into the effective prefactor α.

Finally, substituting eqn (16), (22) and (24) into eqn (15), the energy balance relation is obtained as

$$\frac{1}{2} = \frac{3}{We\beta_{max}} + \frac{3\beta_{max}{}^2}{We}(1 - r\cos\theta_Y) + \sqrt{r}\frac{\alpha\beta_{max}{}^2\sqrt{\beta_{max}-1}}{\sqrt{Re}} \qquad (25)$$

Eqn (25) collapses to $\beta_{max} \propto Re^{1/5}$ scaling when We → ∞ and $\beta_{max} \gg 1$. Overall, this model captures three key pieces of physics: (i) in the fully developed inelastic regime, approximately half the droplet's kinetic energy is lost through a geometric head-loss, (ii) boundary-layer shear dissipates additional energy, with roughness entering through a $\sqrt{r}$ correction to the effective viscous length scale, and (iii) roughness modifies the final surface energy through the Wenzel factor r. This structure captures both hydrodynamic regime changes and substrate microtexture effects. Once the inertial branch is reached (We ≥30), a single fit of the prefactor α enables the model to reproduce the experimental maximum-diameter data with R^2 = 0.98 across the entire high-Weber-number range.

To clarify the relative importance of the different contributions in eqn (25), Fig. 9 compares the order of magnitude of the initial kinetic energy E_k, the total surface-energy change ΔE_S, and the total dissipative contribution E_μ across the present inertial-regime data set. Because the first two terms on the right-hand side of eqn (25) both originate from eqn (22), they are grouped together in Fig. 9 as the single surface-energy contribution ΔE_S, while the third term corresponds to the roughness-amplified viscous dissipation represented by eqn (24).

The plot shows that, over the experimental range considered here, E_k and E_μ are of the same order of magnitude, whereas ΔE_S is consistently smaller, typically by roughly one order of magnitude. This indicates that once the lamella is fully developed (We ≥ 30), the overall spreading dynamics are governed primarily by the balance between inertia and dissipation, with surface energy acting as a secondary correction rather than the dominant contribution. This is consistent with the improved agreement of roughness-independent inertial models at high Weber number, where inertial and dissipative effects dominate the spreading dynamics. Importantly, while ΔE_S acts as a secondary correction in the high-We regime, the model remains fundamentally sensitive to surface topography through the roughness-amplified viscous dissipation term (eqn (24)). By incorporating the Wenzel ratio (r) into the boundary-layer scaling, the model ensures that the primary dissipative pathway continues to reflect the influence of the textured surface, even as the relative importance of surface energy diminishes.

At the same time, although ΔE_S is smaller in absolute magnitude, it remains important in the transitional inertial window, particularly around We ∼ 30–60, where the largest roughness-dependent separation in β_{max} is observed experimentally. In this range, modest variations in the factor $(1 - r\cos\theta_Y)$ are sufficient to produce measurable shifts in

the maximum spreading ratio, even though the dominant energy scale is still set by E_k and E_μ. As We increases further, both E_k and E_μ increase together while the relative influence of ΔE_S weakens, which explains why the sensitivity of β_{max} to roughness decreases at higher Weber number.

The interplay between surface roughness (r), wettability (θ_Y), and the surface-energy contribution in eqn (22) remains important, even though Fig. 9 shows that ΔE_S is generally smaller than both E_k and E_μ in the inertial regime. The principal role of the surface-energy term is therefore not to dominate the overall energy budget, but to provide a roughness- and wettability-dependent correction that becomes most visible in the transitional regime where roughness-induced differences in β_{max} are experimentally resolvable.

For hydrophilic substrates ($\theta_Y < 90^\circ$, $\cos\theta_Y > 0$), increasing r reduces $(1 - r\cos\theta_Y)$ toward zero and can eventually make the surface-energy contribution negative, thereby promoting spreading. This helps explain the larger β_{max} values observed for rougher glass and PETG substrates at intermediate Weber number. On the aluminum substrates, where the effective wettability approaches weak hydrophobicity, the response becomes more complex and lies closer to the validity boundary of the present Wenzel-based framework. In such cases, transient partial-Cassie behavior during the earliest stages of impact may produce small departures from the idealized model.

On the aluminum substrates, the relationship between roughness and spreading becomes more complex as the effective wettability approaches weak hydrophobicity ($\theta_Y > 90^\circ$). While eqn (22) indicates that increasing r should increase resistance to spreading when $\cos\theta_Y < 0$, such conditions lie near the validity boundary of the present Wenzel-based framework because complete liquid penetration of the roughness may become more difficult to maintain during the earliest stages of impact. Accordingly, the hydrophobic aluminum sample (A4) ($\theta_Y = 95^\circ$) is excluded from the Wenzel-based model comparisons in Fig. 10a and 11. For the remaining aluminum samples, the agreement is generally good, although the first two samples (A2 & A3) show minor deviations from the model, which may reflect the fact that their intrinsic wettability lies closer to the hydrophobic limit than for glass or PETG. In such cases, the lamella may be more difficult to fully anchor to the roughened surface during initial spreading, leading to small departures from the idealized Wenzel behavior assumed by the model.

These findings highlight how r, θ_Y, and dynamic wetting states collectively influence spreading behaviors. On hydrophilic substrates, roughness can promote spreading dramatically once $(1 - r\cos\theta_Y)$ becomes negative, while for substrates approaching weak hydrophobicity the response to roughness becomes more sensitive to the degree of liquid conformation to the textured surface during impact. The viscous dissipation term adds further complexity, balancing these competing contributions and underscoring the nuanced yet predictable relationship between maximum spreading, roughness, and wettability.

Fig. 10a shows the comparison of β_{max} obtained through the Laan *et al.*[5] model (eqn (14)) and our experimental data. We include the leftmost cluster of points corresponding to elastic-regime impacts (We < 30) to facilitate comparison with the proposed bimodal framework and to highlight deviations that arise at low Weber numbers. Additionally, Fig. 10b compares the Ukiwe & Kwok[4] model (eqn (1)) prediction against our data set. As expected, neither model accounts for variations in β_{max} associated with changes in surface roughness, leading to systematic deviations from experimental trends at moderate Weber numbers.

Of note, in both cases the data corresponding to a given Weber-number cluster collapses horizontally, reflecting the fact that neither model predicts any variation in β_{max} with surface roughness. This behavior is particularly evident in the cluster

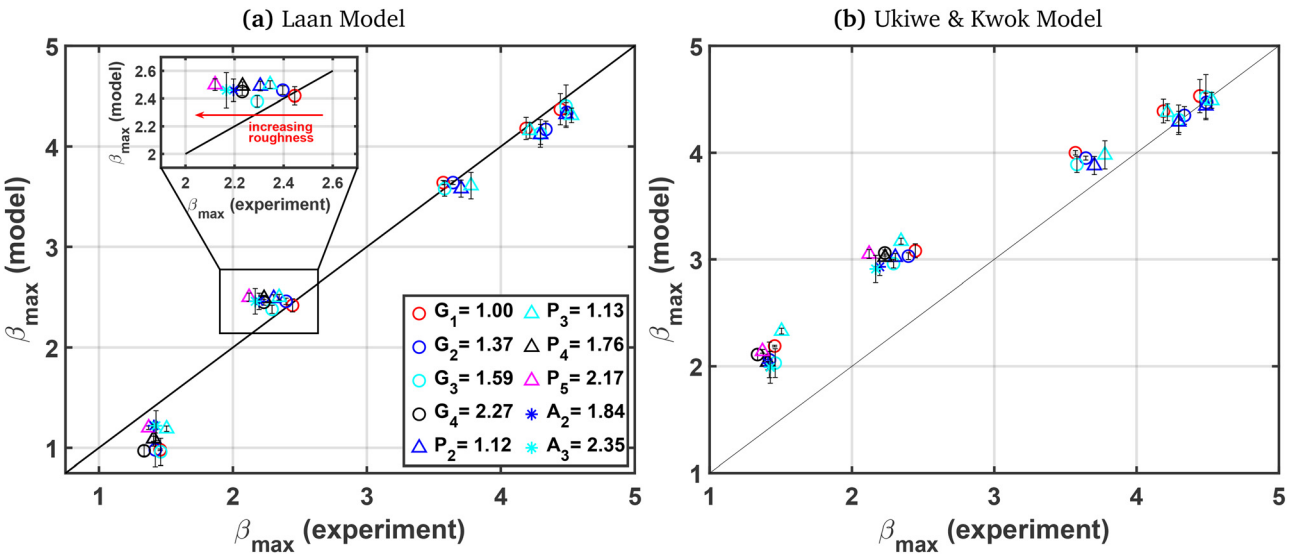

Fig. 10 Comparison of roughness-independent models against the present data: (a) the Laan *et al.* model (eqn (14)) and (b) the Ukiwe & Kwok model (eqn (1)). The leftmost cluster corresponds to elastic-regime impacts (We < 30), while the remaining clusters correspond to inertia-dominated impacts (We ≥ 30).

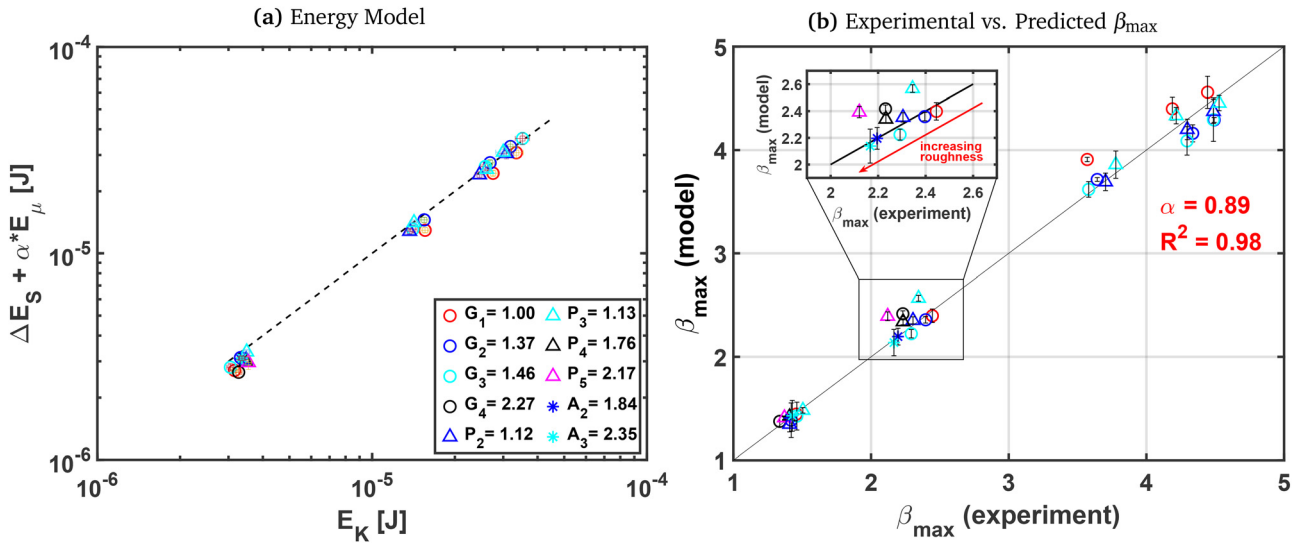

Fig. 11 Comparison of the present roughness-dependent model against the experimental data: (a) log–log plot of $\Delta E_S + \alpha E_\mu$ *versus* E_k, and (b) measured *versus* model-predicted β_{max} using the combined bimodal framework. The leftmost cluster corresponds to elastic-regime impacts (We $<$ 30), while the remaining clusters correspond to inertia-dominated impacts (We $\geq$ 30). Using the single fitted inertial-regime prefactor α = 0.89, the corresponding coefficient of determination in the inertial regime is R^2 = 0.98. Validation of the elastic-regime model is presented separately in Fig. 7.

centered around We $\sim$ 40, where experimental results show the largest spread in β_{max} between smooth and rough substrates.

In contrast, our proposed roughness-dependent bimodal model provides a unified predictive framework for hydrophilic substrates across both elastic and inertial impact regimes. It captures the physics in the very low We regime while also taking roughness into account by incorporating the Wenzel roughness term, such that such that both theory and experimental β_{max} are showing the importance of r and we can obtain accurate estimations of β_{max} for either physical regime of We impacts.

Fig. 11a plots the combined surface–energy and viscous terms, $\Delta E_S + \alpha E_\mu$, against the initial kinetic energy E_k on log–log axes, using the best-fit value α = 0.89. In the inertial regime (We $\geq$ 30), where eqn (25) applies, every point falls very near the 45° line, giving an overall R^2 = 0.98. For completeness, and having previously computed the Laan R^2 over 1 $<$ We $<$ 420, we also computed the Laan R^2 over the inertial-range subset (We $\geq$ 30), obtaining 0.97, hence our roughness-sensitive model yields tighter agreement with the data than the Laan model. While the overall coefficient of determination for the present model is slightly higher than that of the Laan model, the primary improvement lies not in a marginal increase in R^2, but in the ability to capture roughness-dependent trends at moderate Weber numbers that are not resolved by roughness-independent formulations.

Additionally, all points lie close to the $x = y$ line, reinforcing that with α fixed, the model reallocates the initial kinetic reservoir almost perfectly between surface creation, viscous heating and the prescribed 50% head loss. The slight deviations between the model and the data are attributed to its sensitivity to the r value, and the unaccounted role of the compressed gas underneath the droplet impacting the energy balance. To validate this hypothesis, droplet impact tests would have to be repeated under low atmospheric conditions to eliminate the role of the surrounding air in the droplet's impact and spreading dynamics.

Fig. 11b compares the theoretical β_{max} obtained from both eqn (12) and (25) to experimental measurements for a wide set of impacts (1 $<$ We $<$ 420, 1 $<$ r $<$ 7). The leftmost cluster in Fig. 11b (β_{max} $<$ 2, corresponding to We $<$ 30) demonstrates that the elastic sub-model (eqn (12)) reproduces the low-We behavior without introducing additional parameters. Most points cluster tightly along the 45° line, confirming that the combination of head loss and and roughness-amplified boundary-layer dissipation term captures the dominant physics once We is well into the inertial regime. Systematic deviations nevertheless emerge around the transitional window We $\sim$ 30–40. In this cluster the model tends to over predict the spread by 10–15%, consistent with the notion that the lamella is not yet fully developed: the boundary layer is still thick compared to the lamella and the rim is developing, so shear is distributed differently from the uniform disk assumption. At higher Weber numbers (We $\geq$ 50) theoretical and experimental diameters converge again, indicating that roughness amplified viscous work plus the Wildeman *et al.*[7] head loss can indeed explain the energy budget of mature "pizza shaped" impacts.

Taken together, these results indicate that inertia-dominated droplet spreading is largely insensitive to surface properties at sufficiently high Weber numbers, while roughness-induced effects remain relevant in the transitional regime. By explicitly incorporating surface roughness into the energy balance, the present model extends existing approaches to capture these secondary effects without compromising predictive capability in the high-Weber-number limit.

5 Conclusion

This study investigated the impact behavior of droplets on laser-etched surfaces with varying roughness amplitudes (R_a) and wettability properties across a range of Weber (We) and

Reynolds (Re) numbers. The results demonstrate that surface roughness influences droplet impact dynamics, particularly the maximum spreading ratio (β_{max}), with its effect being most pronounced at low and intermediate Weber numbers. Importantly, the significance of roughness here is not that it produces a dramatic shift in β_{max} across the full Weber-number range, but that it causes a consistent and appreciable separation in the transitional regime, especially around We $\sim$ 40. As highlighted by the inset of Fig. 10a, increasing roughness in this regime produces a clear divergence from the roughness-independent Laan model, whereas Fig. 11b shows that the revised roughness-dependent model captures the corresponding roughness-dependent separation in β_{max}. At higher Weber numbers (We $\geq$ 50), the curves move closer together again as inertial effects dominate, which is fully consistent with the limited but still meaningful role of roughness observed experimentally.

Glass and PETG substrates exhibited a decrease in advancing contact angle (θ_a) with increasing surface roughness, while aluminum showed an increase due to its transition toward hydrophobicity. Notably, aluminum's roughest surfaces exhibited partial Cassie states during impact, influencing β_{max} behavior and highlighting the complexity of dynamic wetting states.

This work proposed a two-branch roughness-sensitive model for predicting β_{max}: an elastic branch valid for We $<$ 30 and an inertial, energy-based branch for We $\geq$ 30. In the inertial regime (We $\geq$ 30), a single prefactor α = 0.89 yields R^2 = 0.98, compared to R^2 = 0.97 for the Laan *et al.* correlation over the same range and R^2 = 0.85 when that correlation is applied over the full 1 $<$ We $<$ 420 data set. The model incorporates the influence of roughness through both viscous boundary-layer scaling ($\sqrt{r}$) and the solid–liquid interfacial surface energy term ($1 - r\cos\theta_Y$), capturing the coupled effects of surface texture and effective wettability.

Overall, while the Laan model offers a compact and effective predictor for droplet spreading on smooth and weakly textured surfaces, the present results show that its applicability diminishes for more strongly roughened substrates, particularly in the transitional Weber-number regime. By explicitly incorporating surface roughness into the energy balance, the present framework extends existing scaling approaches while preserving analytical clarity, providing a unified, physically grounded description of droplet impact on textured hydrophilic surfaces.

These findings emphasize the importance of accounting for surface roughness and dynamic wetting behavior when modeling droplet impact phenomena. Future studies could further explore the role of partial Cassie states, transient lamella development, and droplet–air interactions during impact, as well as extend this framework to other liquid–substrate systems. Such insights could inform the design of textured surfaces for applications requiring precise control of droplet behavior, including inkjet printing, spray cooling, and water repellency.

Author contributions

J. G. and C. K. designed and fabricated the laser-etched substrates and carried out all droplet-impact experiments. J. G. and J. B. B. developed the theoretical model for the maximum-spreading ratio. J. G. and J. B. B. wrote the manuscript with input from all authors. O. C. D. supervised the project and secured funding.

Conflicts of interest

There are no conflicts to declare.

Data availability

The data supporting this article have been included as part of the supplementary information (SI). The SI file provides details on the statistical robustness of the bimodal framework, comparative evaluations against existing empirical power-law models, laser texturing fabrication parameters, and comprehensive experimental datasets of the droplet impact dynamics across the different substrates. See DOI: https://doi.org/10.1039/d6sm00167j.

Acknowledgements

This work was made possible by the use of Virginia Tech's Materials Characterization Facility, which is supported by the Institute for Critical Technology and Applied Science, the Macromolecules Innovation Institute, and the Office of the Vice President for Research and Innovation.

References

1 C. Josserand and S. T. Thoroddsen, *Annu. Rev. Fluid Mech.*, 2016, **48**, 365–391.
2 D. H. Kwon, H. K. Huh and S. J. Lee, *Exp. Fluids*, 2013, **54**, 1–11.
3 M. Pasandideh-Fard, Y. Qiao, S. Chandra and J. Mostaghimi, *Phys. Fluids*, 1996, **8**, 650–659.
4 C. Ukiwe and D. Y. Kwok, *Langmuir*, 2005, **21**, 666–673.
5 N. Laan, K. G. de Bruin, D. Bartolo, C. Josserand and D. Bonn, *Phys. Rev. Appl.*, 2014, **2**, 044018.
6 J. Eggers, M. A. Fontelos, C. Josserand and S. Zaleski, *Phys. Fluids*, 2010, **22**, 062101.
7 S. Wildeman, C. W. Visser, C. Sun and D. Lohse, *J. Fluid Mech.*, 2016, **805**, 636–655.
8 S. Moitra, M. Elsharkawy, A. Russo, S. Sarkar, R. Ganguly, P. Asinari and C. M. Megaridis, *Droplet*, 2023, **2**, e63.
9 C. Zhao, Y. Suh and Y. Won, *Droplet*, 2024, **3**, e137.
10 R. Lathia, C. D. Modak and P. Sen, *Droplet*, 2023, **2**, e89.
11 V. Vaikuntanathan and D. Sivakumar, *Langmuir*, 2016, **32**, 2399–2409.
12 K. Yokoi, D. Vadillo, J. Hinch and I. Hutchings, *Phys. Fluids*, 2009, **21**, 072102.
13 M. A. Quetzeri-Santiago, A. A. Castrejon-Pita and J. R. Castrejon-Pita, *Sci. Rep.*, 2019, **9**, 15030.
14 S.-C. Zhao, R. de Jong and D. van der Meer, *Phys. Rev. Lett.*, 2017, **118**, 054502.
15 R. K. Singh, P. D. Hodgson, N. Sen and S. Das, *Langmuir*, 2021, **37**, 3038–3048.

16 D. Richard and D. Quéré, *Europhys. Lett.*, 2000, **50**, 769.
17 K. Okumura, F. Chevy, D. Richard, D. Quéré and C. Clanet, *Europhys. Lett.*, 2003, **62**, 237.
18 J. B. Lee, N. Laan, K. G. de Bruin, G. Skantzaris, N. Shahidzadeh, D. Derome, J. Carmeliet and D. Bonn, *J. Fluid Mech.*, 2016, **786**, R4.
19 R. Rioboo, M. Marengo and C. Tropea, *Exp. Fluids*, 2002, **33**, 112–124.
20 Y. Renardy, S. Popinet, L. Duchemin, M. Renardy, S. Zaleski, C. Josserand, M. Drumright-Clarke, D. Richard, C. Clanet and D. Quéré, *J. Fluid Mech.*, 2003, **484**, 69–83.
21 R. Rioboo, C. Tropea and M. Marengo, *Atom. Sprays*, 2001, **11**(2), 155–165.
22 M. Remacle, A. Ricci-Maccarini, N. Matar, G. Lawson, F. Pieri, V. Bachy and M.-C. Nollevaux, *Eur. Arch. Otorhinolaryngol.*, 2012, **269**, 917–921.
23 I. Langmuir, *Trans. Faraday Soc.*, 1920, **15**, 62–74.
24 Y. Wang, X. Zhao, C. Ke, J. Yu and R. Wang, *Colloid Interface Sci. Commun.*, 2020, **35**, 100256.
25 W. Pfleging, R. Adamietz, H. J. BrÃ¼ckner, M. Bruns and A. Welle, Proc. Laser-Based Micro- and Nanopackaging and Assembly, San Diego, 2007, pp. 51-62.
26 X. Yan, Z. Huang, S. Sett, J. Oh, H. Cha, L. Li, L. Feng, Y. Wu, C. Zhao and D. Orejon, *ACS Nano*, 2019, **13**, 4160–4173.
27 A. Riveiro, P. Pou, J. Del Val, R. Comesana, F. Arias-González, F. Lusquinos, M. Boutinguiza, F. Quintero, A. Badaoui and J. Pou, *Proc. CIRP*, 2020, **94**, 879–884.
28 C. Clanet, C. Beguin, D. Richard and D. Quéré, *J. Fluid Mech.*, 2004, **517**, 199–208.
29 I. V. Roisman, *Phys. Fluids*, 2009, **21**, 052104.